Electromagnetic Parameters of a Three Phase Transverse Flux Machine with an External Rotor for Wheel Hub Drives

Erich Schmidt[1], Daniel Brunnschweiler, Stefan Berchten[2]

[1]Institute of Electrical Drives and Machines
Vienna University of Technology, Vienna, Austria

[2]MagnetDrives AG, Zug, Switzerland

Abstract – **The transverse flux machine with a permanent magnet excited rotor is one of the most important machine topology for the application with electric driven vehicles. In particular with wheel hub drive systems, the design of such a machine with an external rotor is favourably against conventional induction machines due to the high output torque in conjunction with low heat losses. The paper discusses 3D finite element analyses of a novel design of a three phase transverse flux machine with an external rotor. In order to setup an environment suitable for a prototype design of the single sided transverse flux machine, special attention has to be given to modelling as well as analysis methods. The results presented here are focussed on the most important electromagnetic parameters such as no-load voltages, short-circuit currents and electromagnetic torque.**

Index Terms – **Transverse flux machine, Permanent magnet machine, Finite element analysis**

I. Introduction

In general, two different topologies of a transverse flux machine exist [1]–[5]. Thereby, double-sided arrangements can be used only in either single phase or two phase mode. On the other hand, single-sided arrangements can be designed for three phase mode, too.

In contrast to conventional induction machines with more than one phase, there is no common rotating field with all designs of transverse flux machines [1]–[6]. In order to produce a resulting shaft torque as comparatively as smooth as with conventional induction machines, either stator or rotor parts have to be mechanically shifted according to the number of phases. Nevertheless, the alternating fields with an electrical angular shift according to the number of phases cause higher harmonics with the electromagnetic torque as well as noticeable shear stresses in all carrier parts and the shaft [6].

The novel single-sided design with its main data listed in Table I consists of a three phase arrangement with an external rotor. Fig. 1 depicts two poles of the basic arrangement of one single phase whereas Fig. 2 illustrates two poles of the complete three phase arrangement. The rotor parts of the three phases are arranged in line and carry the permanent magnets with an alternating magnetization in circumferential direction. The stator parts of the three phases carry the ring windings of the three phases and have an appropriate mechanical angular shift necessary for the three phase operation.

TABLE I
Main Data of the Transverse Flux Machine

Number of poles	120	
Rated speed	400	rpm
Maximum speed	1200	rpm
Outer stator diameter	380	mm
Outer rotor diameter	410	mm
Airgap length	1	mm
Total axial length	100	mm
Rated stator current	120	A
Remanent flux density	1.30	T
Coercive field strength	985.25	kA/m

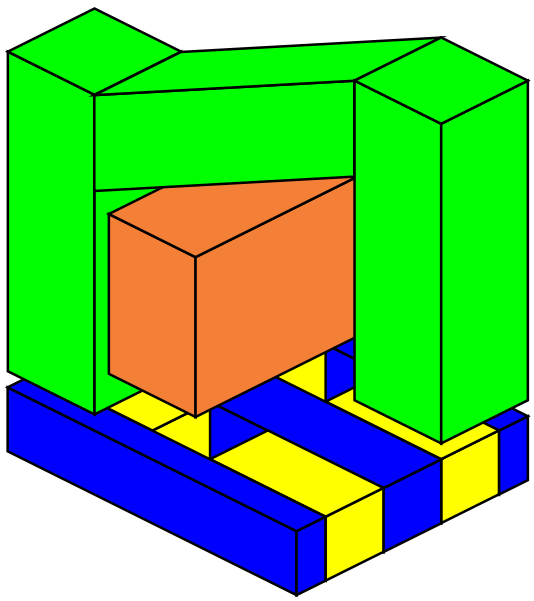

Fig. 1: Basic arrangement of two poles of a single sided transverse flux machine with flux concentration

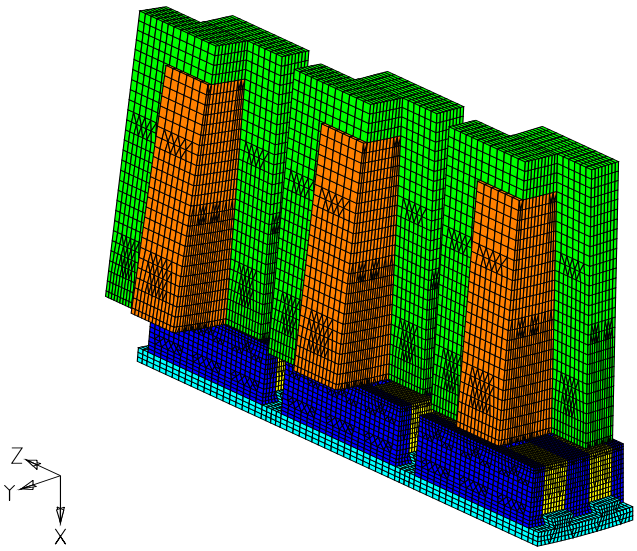

Fig. 2: Three phase transverse flux machine with in line rotor segments and inserted permanent magnets as well as shifted stator segments and ring windings, finite element model of two poles

II. Finite Element Modelling

The finite element model as shown in Fig. 2 consists of completely independent stator as well as rotor parts and includes only two poles of the machine as the smallest necessary part. In order to reflect the periodicity of the magnetic field, appropriate repeating periodic boundary conditions for the unknown degrees of freedom of the 3D magnetic vector potential are applied at the boundaries being two poles pitches apart.

The various nonlinear finite element analyses utilize a 3D vector potential formulation with an incorporated Coulomb gauge

$$\operatorname{curl}\Big(\underset{\sim}{\nu}\cdot\operatorname{curl}\mathbf{A}\Big)=\mathbf{J}\ ,\quad \operatorname{div}\mathbf{A}=0 \tag{1}$$

with appropriate Neumann and Dirichlet boundary conditions

$$\Big(\underset{\sim}{\nu}\cdot\operatorname{curl}\mathbf{A}\Big)\times\mathbf{n}=\mathbf{K}\ \text{ on }\Gamma_H\ , \tag{2a}$$

$$\mathbf{A}\times\mathbf{n}=\mathbf{0}\ \text{ on }\Gamma_B\ , \tag{2b}$$

where $\underset{\sim}{\nu}$ denotes an anisotropic reluctivity tensor, Γ_H the boundary where $\mathbf{n}\times\mathbf{H}$ is specified and Γ_B the boundary where $\mathbf{n}\cdot\mathbf{B}$ is specified [7]–[9].

Regarding the arrangement as depicted in Fig. 2, the nonlinear anisotropic material properties of the laminated stator and rotor iron regions are described by

$$\underset{\sim}{\nu}_{r\varphi z}(\mathbf{B})=\begin{bmatrix}\nu_{rr}(\mathbf{B}) & 0 & 0\\ 0 & \nu_{\varphi\varphi}(\mathbf{B}) & 0\\ 0 & 0 & \nu_{zz}(\mathbf{B})\end{bmatrix}\ , \tag{3}$$

$$\nu_{\varphi\varphi}(\mathbf{B})=\big(1-k_F\big)\,\nu_0+k_F\,\sqrt{\nu_{rr}(\mathbf{B})\,\nu_{zz}(\mathbf{B})}\ ,$$

where k_F denotes the stacking factor of the laminations.

With an intent of investigating cross-coupling effects between the three phases, Dirichlet boundary conditions of the magnetic vector potential on the symmetry planes between the phases in axial direction can be used optionally. With these internal boundary conditions, the magnetic flux densities are only tangential on these symmetry planes yielding fully decoupled phases. Without any coupling of the three phases, they will act independently in particular on the electromagnetic torque. On the other hand, there exist additional axial stray flux portions between the three phases. In dependence on the axial distance of the three phases, these flux portions will influence the evolved electromagnetic torque with both no-load and load cases.

The injection of the three phase currents with the ring windings of the stator follows

$$i_1(\varphi)=\hat{I}\,\cos\Big(\beta+\varphi+\varphi_0\Big)\ , \tag{4a}$$

$$i_2(\varphi)=\hat{I}\,\cos\Big(\beta+\varphi+\varphi_0-\frac{2\pi}{3}\Big)\ , \tag{4b}$$

$$i_3(\varphi)=\hat{I}\,\cos\Big(\beta+\varphi+\varphi_0-\frac{4\pi}{3}\Big)\ , \tag{4c}$$

where φ_0 denotes the initial angular rotor position of the first phase. As shown in Fig. 2, stator and rotor of the first phase are arranged in an unaligned position which is represented by $\varphi_0=\pi/2$. Moreover, β denotes the current angle with respect to the rotor fixed coordinate system. Thereby, current angles of $\beta=0$ or $\beta=\pm\pi$ produce no resultant torque. A maximum resultant torque is generated with a current angle of $\beta=\pm\pi/2$ [6].

The various angular rotor positions are now calculated by utilizing the sliding surface approach in conjunction with a domain decomposition algorithm [6], [10]–[12]. Thereby, the independent stator and rotor parts Ω_{st} and Ω_{rt} have an equidistant mesh discretization in circumferential direction on a cylindrical sliding surface Γ_{sl} within the air-gap while the mesh discretization in axial direction coincides between both parts.

The two independent model parts are now described with their own symmetric stiffness matrices $\mathbf{K}_{st}$,$\mathbf{K}_{rt}$ and by the matrix equations

$$\mathbf{K}_m\,\mathbf{U}_m+\mathbf{G}_m=\mathbf{P}_m\ ,\quad m=\{st,rt\}\ , \tag{5}$$

wherein $\mathbf{G}_{st}$,$\mathbf{G}_{rt}$ summarize the boundary terms related to unknown tangential components of the magnetic field strength at the sliding surface boundary Γ_{sl}. Afterwards, the stiffness matrices of the model parts are decomposed according to two exclusive subsets of interior (i) and exterior (e) unknown degrees of free-

dom,

$$\begin{bmatrix} \mathbf{K}_{m,ii} & \mathbf{K}_{m,ie} \\ \mathbf{K}_{m,ie}^T & \mathbf{K}_{m,ee} \end{bmatrix} \begin{bmatrix} \mathbf{U}_{m,i} \\ \mathbf{U}_{m,e} \end{bmatrix} + \begin{bmatrix} \mathbf{0} \\ \mathbf{G}_{m,e} \end{bmatrix} = \begin{bmatrix} \mathbf{P}_{m,i} \\ \mathbf{P}_{m,e} \end{bmatrix} . \quad (6)$$

The coupling of the two model parts is now provided by a direct mapping of the degrees of freedom along the sliding surface boundary Γ_{sl} between stator and rotor parts depending on the angular rotor position,

$$\mathbf{U}_{rt,e} = \mathbf{E}_k \, \mathbf{U}_{st,e} \ , \quad \mathbf{G}_{st,e} = -\mathbf{E}_k^T \, \mathbf{G}_{rt,e} \ . \quad (7)$$

According to the used discretization in circumferential direction, this locked-step coupling allows for angular positions with an electrical increment of $\Delta\varphi = \pi/24$.

Therefore, the finite element mesh remains completely unchanged for all angular rotor positions without any remeshing. Consequently, different numerical errors with respect to the angular rotor position are avoided. Additionally, distinct decompositions of the smaller stiffness matrices $\mathbf{K}_{m,ii}$ of the two independent model parts significantly reduce the calculation times for various rotor positions even in a nonlinear analysis.

III. Analysis Results

A. No-Load Voltages and Short-Circuit Currents

Fig. 3 and Fig. 4 show the no-load voltages of the three phases with a Y-connected stator for the rated speed of $n = 400\,\text{rpm}$, respectively. Further, Fig. 5 shows the symmetrical short-circuit currents of the three phases with a Y-connected stator for the rated speed of $n = 400\,\text{rpm}$.

Caused by the high level of saturation, the no-load voltages contain a significant 3rd harmonic component resulting in a non-vanishing sum of the three phase voltages as drawn additionally. In comparison of the coupling effects, the fundamental harmonic decreases from 206.4 V to 203.2 V for decoupled and coupled phases. On the other hand due to the low level of saturation, the symmetrical three phase short-circuit currents are nearly sinusoidal with respect to time. Thereby, the short-circuit currents are smaller with coupled against decoupled phases.

B. Electromagnetic Torque

As described in [6], the torque calculation requires only the portions along a cylindrical surface within the air-gap. Hence, the electromagnetic torque is evaluated from the analysis results by summarizing the circumferential component of the Maxwell stress vector

$$p_{\varphi,mn} = \nu_0 \, B_r(r_T, \varphi_m, z_n) \, B_\varphi(r_T, \varphi_m, z_n) \quad (8)$$

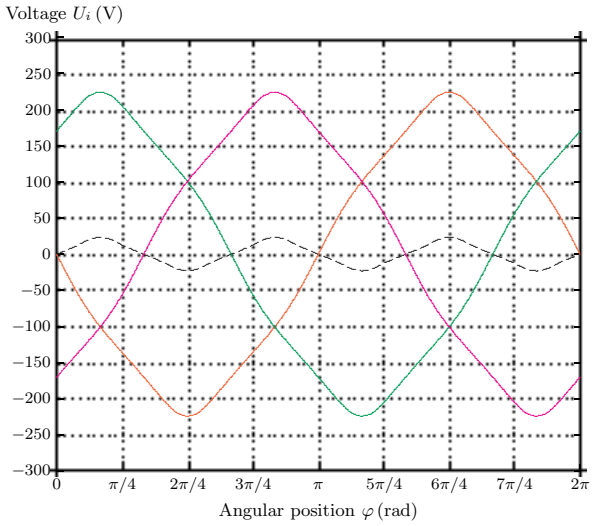

Fig. 3: No-load voltages of the three phases, rated speed of $n = 400\,\text{rpm}$, decoupled phases

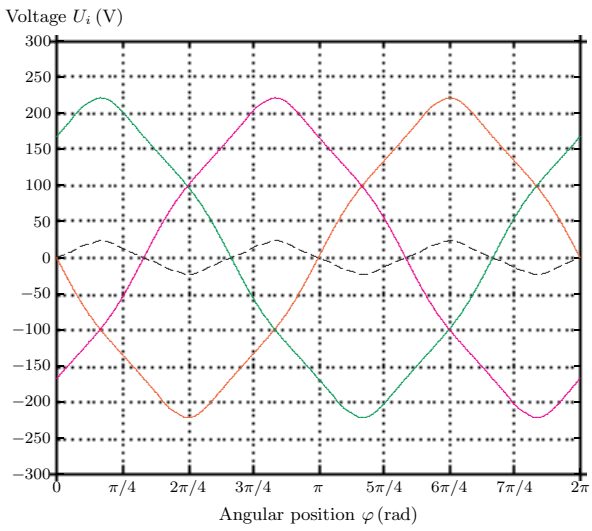

Fig. 4: No-load voltages of the three phases, rated speed of $n = 400\,\text{rpm}$, coupled phases

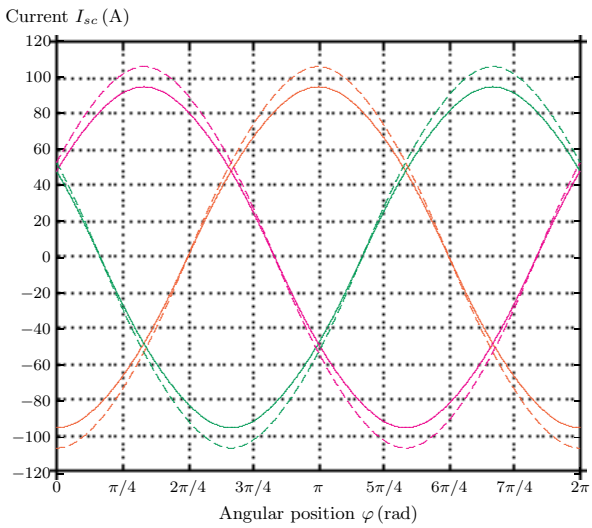

Fig. 5: Short-circuit currents of the three phases, rated speed of $n = 400\,\text{rpm}$, decoupled phases (dashed lines) and coupled phases (solid lines)

along a cylindrical surface within the air-gap as

$$T_z = p \sum_{n=1}^{N_z} \sum_{m=1}^{N_\varphi} \frac{r_T \, \Delta v_{mn}}{\Delta r_T} \, p_{\varphi,mn} \quad , \tag{9}$$

where p is the number of pole pairs, N_φ and N_z denote the numbers of air-gap elements in circumferential and axial direction, r_T and Δr_T are radius of center of gravity and radial thickness of each hexahedral air-gap element along the cylindrical surface, and Δv_{mn} denote the finite element volume, respectively.

Fig. 6 and Fig. 7 show the cogging torque of the three phases and the entire machine with decoupled and coupled phases. Fig. 8 and Fig. 9 show the load torque of the three phases and the entire machine with the rated stator current of $\hat{I} = 120\,\mathrm{A}$ in the quadrature axis according to a maximum electromagnetic torque with decoupled and coupled phases.

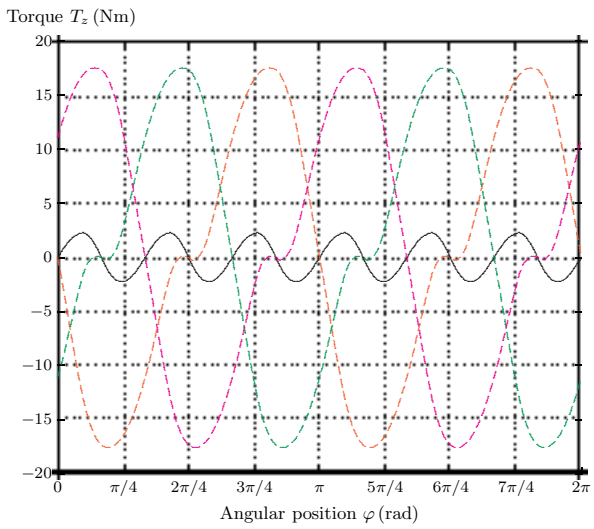

Fig. 6: Cogging torque of the three phases and the entire machine, decoupled phases

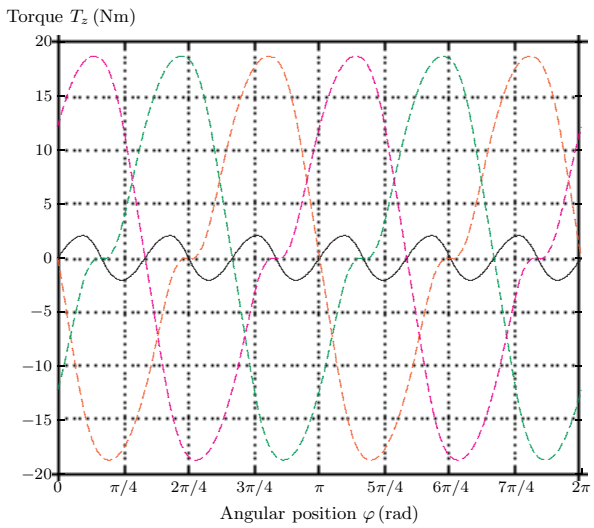

Fig. 7: Cogging torque of the three phases and the entire machine, coupled phases

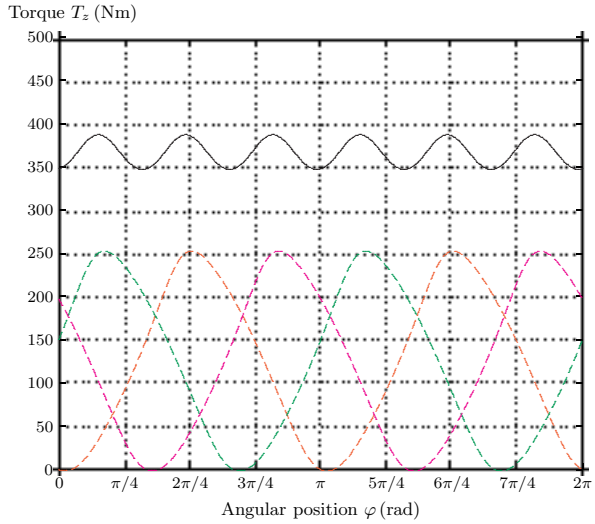

Fig. 8: Load torque of the three phases and the entire machine with rated stator current of $\hat{I} = 120\,\mathrm{A}$, decoupled phases

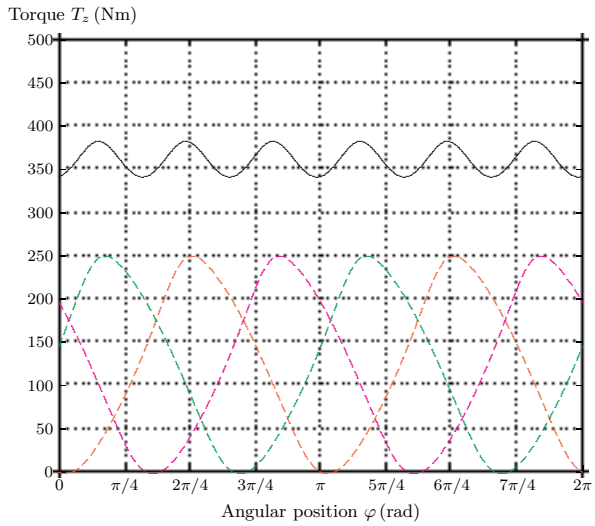

Fig. 9: Load torque of the three phases and the entire machine with rated stator current of $\hat{I} = 120\,\mathrm{A}$, coupled phases

Fig. 10 and Fig. 11 show the load torque of the entire machine with various quadrature axis stator currents of $\hat{I} = 30\,\mathrm{A} \ldots 150\,\mathrm{A}$ with decoupled and coupled phases, respectively. Corresponding, Table II lists average value and distortion factor

$$\Delta T_z = \frac{T_{z,max} - T_{z,min}}{2\,T_{z,av}} \tag{10}$$

as well as measurement data from an initial prototype.

The three phases contribute to the electromagnetic torque independently with only little interaction. Due to the appropriate electrical shift of the three phase currents, the resulting shaft torque is comparatively as smooth as for conventional three phase induction machines. With coupled against decoupled phases, the cogging torque of the three phases is slightly larger while with the entire machine both cogging torque and average value of the load torque are insignificantly smaller. Nevertheless, the electromag-

netic torque shows higher harmonics with in particular a significant 6th harmonic component which gain in significance with the mechanical construction.

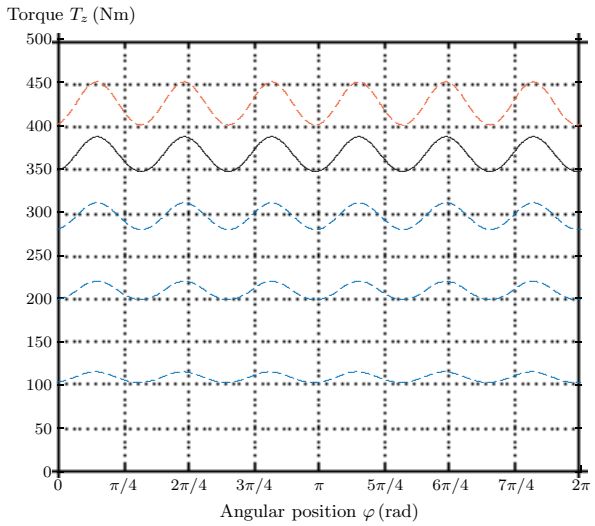

Fig. 10: Load torque of the entire machine with stator currents $\hat{I} = 30\,\text{A} \ldots 150\,\text{A}$, decoupled phases

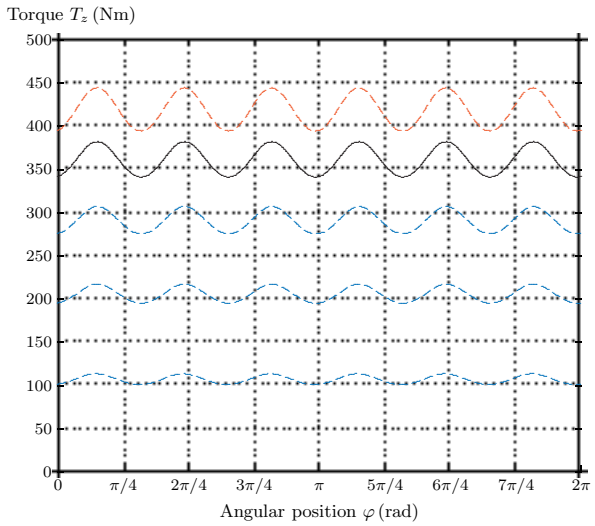

Fig. 11: Load torque of the entire machine with stator currents $\hat{I} = 30\,\text{A} \ldots 150\,\text{A}$, coupled phases

C. Field Results

Fig. 12 and Fig. 13 show the distribution of the radial magnetic flux density within the air-gap of one phase for the aligned and unaligned position of rotor and stator poles for the no-load condition.

With the aligned position, the magnetic flux crosses from stator to rotor along adjacent pole regions of stator and rotor causing a concentration of the radial magnetic flux density within the air-gap along these poles faces. On the other hand with the unaligned position, the magnetic flux crosses from stator to rotor only via small overlapping regions of the pole faces of stator and rotor.

TABLE II
LOAD TORQUE, AVERAGE VALUE, DISTORTION FACTOR AND MEASUREMENT DATA

	Decoupled phases		Coupled phases		
Current load	Average value	Distortion factor	Average value	Distortion factor	Measurement data
$\hat{I}$ (A)	$T_{z,av}$ (Nm)	ΔT_z (1)	$T_{z,av}$ (Nm)	ΔT_z (1)	$T_{z,m}$ (Nm)
30	109	0.0550	107	0.0555	104
60	209	0.0520	206	0.0535	196
90	295	0.0530	291	0.0540	269
120	366	0.0550	361	0.0565	325
150	425	0.0585	419	0.0600	367

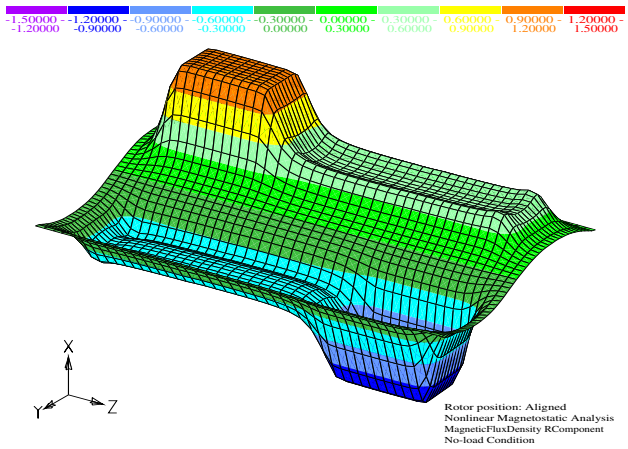

Fig. 12: Distribution of the radial magnetic flux density within the air-gap of one phase, aligned position of rotor and stator poles, no-load condition

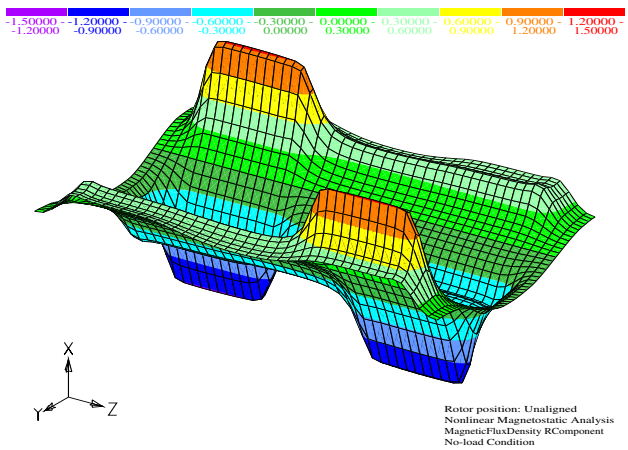

Fig. 13: Distribution of the radial magnetic flux density within the air-gap of one phase, unaligned position of rotor and stator poles, no-load condition

IV. CONCLUSION

The transverse flux machine with a permanent magnet excited rotor is well suited in particular for wheel hub drive applications of electric driven vehicles. The presented novel concept of such a machine with an external rotor consists of a three phase arrangement with

an appropriate mechanical angular shift of the stator parts whereas the rotor parts are arranged in line. All phases contribute to the electromagnetic torque independently with only less interaction. Due to an appropriate electrical shift of the three phase currents in the stator ring windings, the resulting shaft torque is comparatively as smooth as with conventional induction machines.

The 3D finite element analyses of the single sided transverse flux machine use only one single finite element model with completely independent rotor and stator parts for all angular rotor positions. On the sliding surface between both parts, they are modelled with an equidistant finite element discretization with respect to the movement direction of the rotor. The various angular rotor positions are analyzed without any remeshing of air-gap regions by using a domain decomposition algorithm in the nonlinear calculations.

The presented results are focussed on the most important parameters such as no-load voltages, short-circuit currents and electromagnetic torque of this novel prototype design. First measurement results obtained from an initial design show a good agreement with the numerical results discussed herein.

References

[1] Lange A., Canders W.R., Laube F., Mosebach H.: "Comparison of Different Drive Systems for a 75kW Electrical Vehicle Drive". *Proceedings of the International Conference on Electrical Machines, ICEM*, Espoo (Finland), 2000.

[2] Hackmann W.: *Systemvergleich unterschiedlicher Radnabenantriebe für den Schienenverkehr: Asynchronmaschine, permanenterregte Synchronmaschine, Transversalflussmaschine*. Doctoral Thesis (in German), TU Darmstadt, 2003.

[3] Blissenbach R.: *Entwicklung von permanenterregten Transversalflussmaschinen hoher Drehmomentdichte für Traktionsantriebe*. Doctoral Thesis (in German), RWTH Aachen, 2002.

[4] Anpalahan P.: *Design of Transverse Flux Machines using Analytical Calculations and Finite Element Analysis*. Licentiate of Technology Thesis, Royal Institute of Technology, Stockholm, 2001.

[5] Njeh A., Masmoudi A., Elantably A.: "3D Finite Element Analysis Based Investigation of the Cogging Torque of a Claw Pole Transverse Flux Permanent Magnet Machine". *Proceedings of the IEEE International Conference on Electric Machines and Drives, IEMDC*, Madison (WI, USA), 2003.

[6] Schmidt E.: "3D Finite Element Analysis of the Cogging Torque of a Transverse Flux Machine". *IEEE Transactions on Magnetics*, Vol. 41, No. 5, May 2005.

[7] Biro O., Preis K., Richter K.R.: "On the Use of the Magnetic Vector Potential in the Nodal and Edge Finite Element Analysis of 3D Magnetostatic Problems". *IEEE Transactions on Magnetics*, Vol. 32, No. 3, May 1996.

[8] Hameyer K., Belmans R.: *Numerical Modelling and Design of Electrical Machines and Devices*. WIT Press, Southampton, 1999.

[9] Jin J.: *The Finite Element Method in Electromagnetics*. John Wiley & Sons, New York (USA), 2002.

[10] Schmidt E.: "Application of a Domain Decomposition Algorithm in the 3D Finite Element Analysis of a Transverse Flux Machine". *Proceedings of the IEEE Canadian Conference on Electrical and Computer Engineering (CCECE)*, Winnipeg (MB, Canada), 2002.

[11] De Gersem H., Gyselinck J., Dular P., Hameyer K., Weiland T.: "Comparison of Sliding Surface and Moving Band Techniques in Frequency-Domain Finite Element Models of Rotating Machines". *Proceedings of the 6th International Workshop on Electric and Magnetic Fields, EMF*, Aachen (Germany), 2003.

[12] De Gersem H., Weiland T.: "Harmonic Weighting Functions at the Sliding Surface Interface of a Finite Element Machine Model Incorporating Angular Displacement". *IEEE Transactions on Magnetics*, Vol. 40, No. 2, March 2004.